Property Modulation of Graphene Oxide Incorporated with TiO$_2$ for Dye-Sensitized Solar Cells

Amanpal Singh,* Yogesh Kumar Saini, Anuj Kumar, Sanjeev Gautam, Dinesh Kumar, Viresh Dutta, Han-koo Lee, Jongsu Lee, and Sanjay Kumar Swami*

Read Online

| ACCESS | | Metrics & More | | Article Recommendations | | Supporting Information |

ABSTRACT: Graphene oxide (GO) nano-powder is synthesized by the modified Hummer's method, and further thin films are deposited by using the water solution of GO through spin-coating. These films are thermally reduced along with the synthesized GO nano-powder at 50 to 200 °C in a high vacuum. Microstructural, electrical, and optical properties are expectedly controlled by thermal reduction. The electronic properties of GO are investigated by X-ray photoelectron spectroscopy and near-edge X-ray absorption fine structure. The reduction is confirmed by Raman spectroscopy. The work function and band gap of GO are tuned with the thermal reduction. The changes in properties of GO are not linear, and anomalous changes are observed for the reduction around 150 °C. Pristine and reduced GO nano-powder is incorporated into TiO$_2$ paste to be the photoanode for dye-sensitized solar cells (DSSCs). It is observed that the performance of the fabricated cells is significantly enhanced for the GO reduced at 150 °C, and the cell exhibited a significant increment of ∼23% for the power conversion efficiency in comparison to DSSC based on an unmodified TiO$_2$ photoanode.
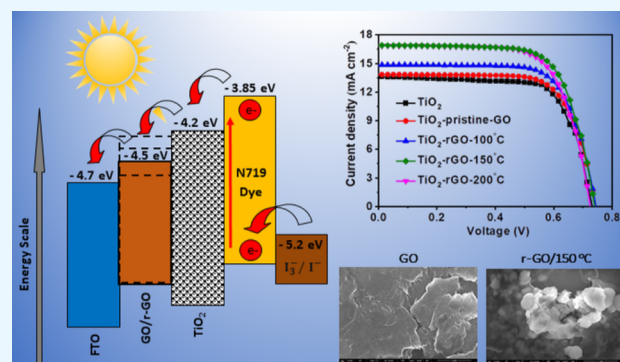
1. INTRODUCTION

Solar energy is one of the favorite kinds of renewable energy, but its popularity is limited due to some extent by the high cost of conventional solar cells. Among different photovoltaics, dye-sensitized solar cells (DSSCs) have gained significant interest due to their light weight, remarkably high power conversion efficiency (PCE), overall low cost, and eco-friendly fabrication.[1] The DSSCs consist of a transparent conducting oxide (TCO) layer; a wide band gap semiconductor as an electron acceptor, which is treated with an organic dye to harvest sunlight; a hole conductor medium, which is often iodide/tri-iodide electrolyte; and a platinum (Pt)-deposited counter electrode (CE).[2] The sensitizer dye molecules absorb sunlight and get into an excited state. The excited dye molecule injects the electrons into the conduction band (CB) of the electron acceptor semiconductor material. It leads to the dye molecule being oxidized. The electrons are collected at the TCO layer and flow through the external circuit to the cathode CE side. These electrons combine with triiodide ions in the electrolyte, which help the oxidized dye molecules to return to the ground state by accepting electrons from iodide ions.[3] Metal oxide wide band gap semiconductors such as ZnO and TiO$_2$ are widely used for photogenerated electron acceptor layers because these can prevent shunting and leakage currents under reverse bias.[1] The film of nanoparticles of mesoporous TiO$_2$ has been identified as an excellent photoanode material due to its superior electrical and optical properties. It serves a dual purpose of providing a high surface area for the photovoltaic sensitizer as well as being a conductor of photogenerated electrons from the sensitizer.[4] Although a mesoporous nanostructure provides a larger surface area for dye, the linkage between these nanoparticles must be improved so the photogenerated electrons can be collected at the cell anode instead of recombining with the oxidized dye molecules present in the TiO$_2$ matrix.[5] Furthermore, nanostructures of TiO$_2$ also contain charge-trapping sites and larger grain boundaries, causing retardation in the charge transport.[5] The incorporation of carbon nanostructures in the TiO$_2$ matrix provides a solution that has been widely investigated recently to overcome the reasons for the inefficiency of DSSCs. These carbanion nanostructures improve the linkage between the TiO$_2$ matrix, leading to faster electron transport, and/or reduce the recombination at the nanoparticle—electrolyte as well as nanoparticle—oxidized dye molecule interface.[6] Graphene has been significantly explored for its applications in solar cells,

such as transparent electrodes and CE in DSSCs. In addition to the transparent electrode and the CE, graphene also has been demonstrated as the electron acceptor and charge transfer medium to improve the efficiency of solar devices.[7−9] Yang et al.[9] added graphene as a 2D bridge into the nanocrystalline electrodes of DSSCs and found that the short-circuit current density (J_{SC}) improved without losing the open-circuit voltage (V_{OC}). The nanocrystalline TiO_2 could anchor on the graphene flake trimly to form graphene bridges across several intermolecular forces, such as physisorption and electrostatic binding. Additionally, due to its excellent electrical conduction, the bridged graphene behaves as an electron transfer medium to quickly improve the electron transport from the CB of TiO_2 at the anchor position, leading to the suppression of the recombination of photogenerated electrons.

The GO is a solution-processable hydrophilic allotrope of graphene. The GO is less conducting but offers several advantages over pristine graphene as being amenable to solution-based processes, making it easy to deposit as a thin film, with low-cost synthesis, ease of material processing, mechanical flexibility, adhesion compatibility with several substrates, and so forth. Furthermore, the high work function of GO creates a large energy level offset at the interface, leading to efficient charge separation.[10] The typical structure of the fabricated DSSCs with a charge flow scheme is shown in Figure S1 (Supporting Information). In the DSSC structure, the mixing of GO flakes with TiO_2 paste provides a better Brunauer−Emmet−Teller (BET) area and further improves charge transportation.[11] The detailed photovoltaic parameters of the DSSC with GO, synthesized using different techniques as reported in the literature, are provided in Table S1 in the Supporting Information.

The reduction of GO led to be change in the CB energy level, and hence by controlling the reduction of GO, the electronic and optical properties of GO can be tuned in the desired way. Thermal annealing in the vacuum provides better control over reduction in comparison to chemical reduction processes.[12−14]

This paper reports on the studies of GO synthesized by the Hummers method and the nanostructures of reduced GO (rGO) achieved by thermal annealing of GO in the vacuum of $\sim10^{-6}$ mbar at 50, 100, 150, and 200 °C. The GO is used in DSSCs to prove the enhancement in the device's performance.

2. EXPERIMENTAL SECTION

2.1. Synthesis of GO Nano-Powder. The GO was prepared via the modified Hummers method.[11,15] Fine mesh 2 g graphite powder (~6 nm) was stirred with 2 g $NaNO_3$ in 98% concentrated sulfuric acid (92 mL) for 1 h at 0 °C. Further, 12 g $KMnO_4$ was gradually mixed in intervals, keeping the temperature below 10 °C, and the mixture was then stirred at 60 °C for 90 min. The final solution was diluted with 50 ml of water, which caused the heating of the solution to 90 °C. The reaction was terminated by adding 150 mL de-ionized (DI) water and 30% H_2O_2 solution (10 mL). This solution was filtered and washed using a 5% HCl aqueous solution. Finally, it was washed three times with DI water. The resulting GO powder was dried in a dark and cool place. The powder was slowly crushed into fine particles with the help of a mortar and pestle. Thus, the obtained powder was equally divided into five parts, and keeping the pristine one untouched, the other parts were reduced to 50, 100, 150, and 200 °C in high vacuum. All

these powders were ready for further use to prepare the DSSC photoanode.

2.2. Deposition of GO and rGO Thin Films. The pristine GO powder was mixed ultra-sonically in the DI water for use for film deposition. Multi-layered films were deposited on the corning glass and fluorene-doped tin oxide (FTO) substrates by a spin coater at 2000 rpm. The deposited films were divided into equal pieces for further thermal reduction in high vacuum ($\sim10^{-6}$ mbar) at four different temperatures: 50, 100, 150, and 200 °C. All the thin films were characterized in detail to investigate the properties of GO and rGO and to establish the correlation with the DSSC performance.

2.3. Preparation of Photoanode. The photoanode was prepared by adding 5 wt % GO and rGO in TiO_2 paste (18NR-T, Dyesol) by grinding method and then doctor blading for the desired thickness on FTO glass substrates (7 Ω/□). Fabrication of the DSSCs using N719 dye and iodine electrolyte has been reported in our earlier publication.[16] TiO_2 photoanodes were dipped in a 0.5 mM N719 dye (Dyesol) solution for ~20 h at room temperature in the dark. Afterward, the photoanodes were washed with ethanol. Platinum CE was prepared using H_2PtCl_6 in ethanol.[17] Subsequently, photoanode and platinum CE were sealed using 25 μm Surlyn. The iodine electrolyte was filled via predrilled holes in CE using the vacuum pump. The active area of the device was 0.25 cm². Details of the characterization techniques are available in the Supporting Information.

2.4. Characterization Techniques. The GO and rGO samples are characterized via X-ray diffraction (XRD), Raman, X-ray photoelectron, near-edge X-ray absorption fine structure (NEXAFS), and UV−vis spectroscopy. Topography and morphology were investigated by scanning Kelvin probe microscopy (SKPM) and field emission scanning electron microscopy (FESEM). The detail of these characterization instruments is provided in the Supporting Information.

3. RESULTS AND DISCUSSION

3.1. Reduction Tuning of Graphene Oxide. Figure 1 shows the XRD pattern of rGO films along with that of pristine GO films.

The deposited films are in (001) orientation. A sharp and intense peak at 2θ = 10.211° with the (001) plane was observed with full width at half maxima (fwhm) 1.318° for the

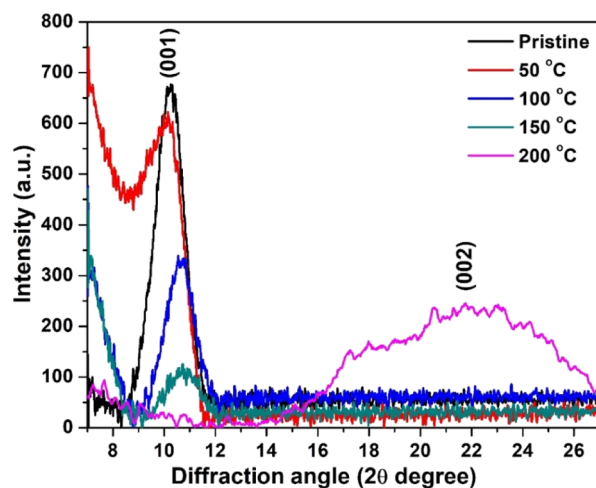**Figure 1.** XRD pattern of pristine and rGO thin films.
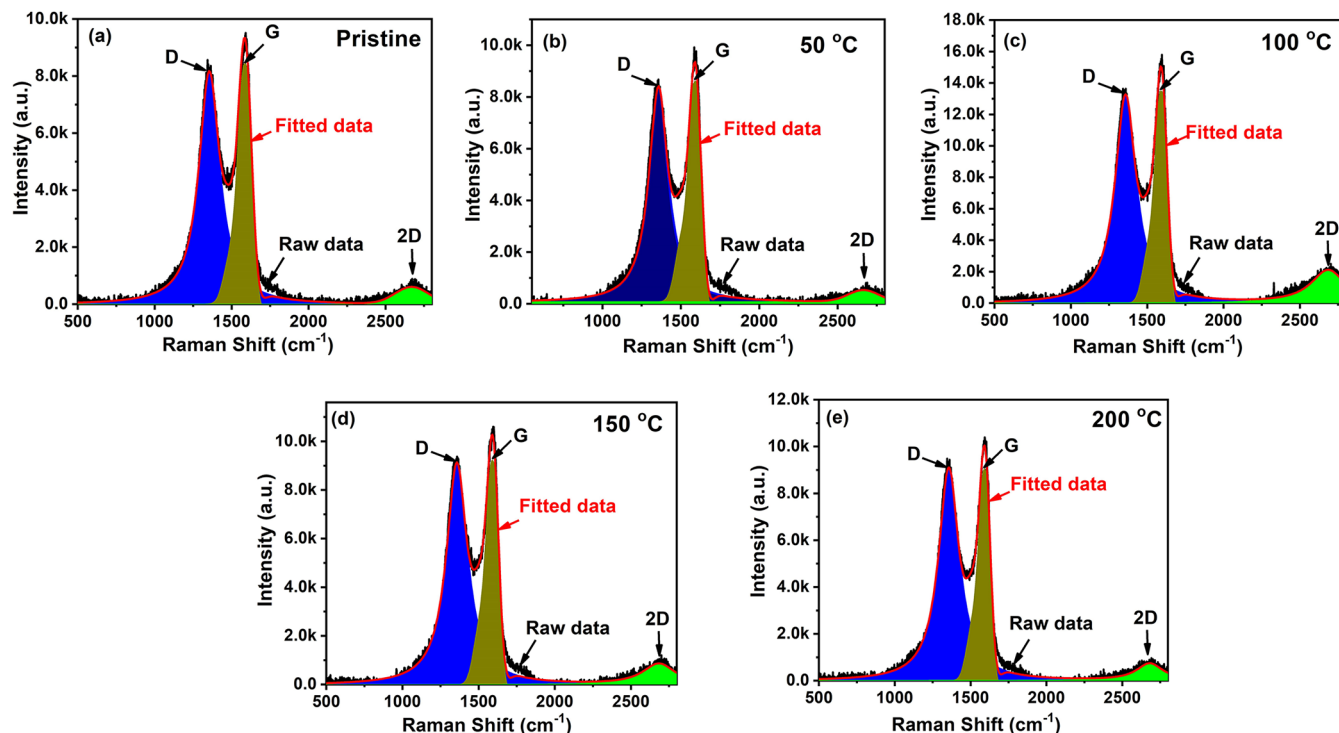
Figure 2. Raman spectra of GO thin films (a) pristine, and reduced at (b) 50, (c) 100 (d) 150, (e) 200 °C.
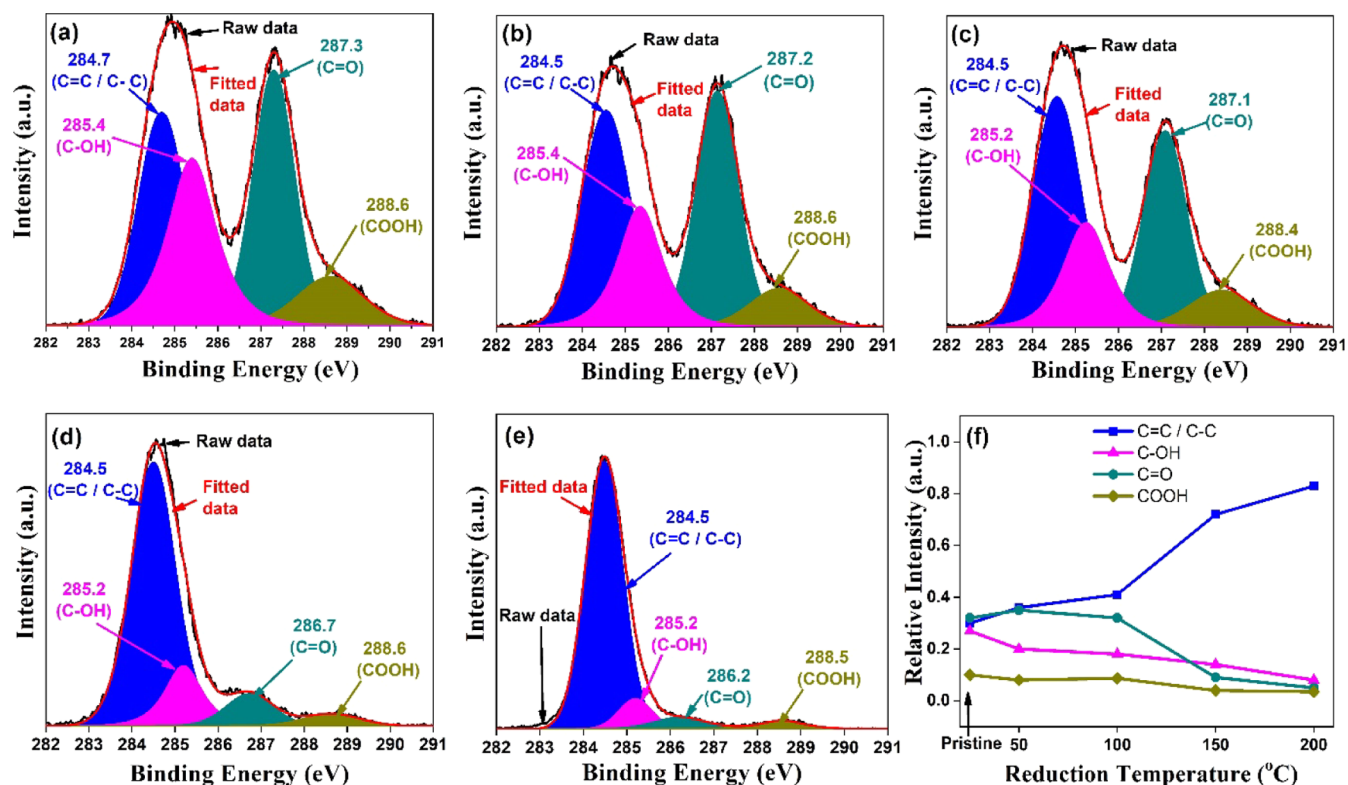

Figure 3. Deconvoluted high-resolution C_{1s} spectra for (a) pristine and the samples reduced at (b) 50, (c) 100 (d) 150, and (e) 200 °C; (f) reduction dependence of the relative contribution of C_{1s} peak components.

pristine sample; meanwhile, this peak was observed at 10.148, 10.631, and 10.742° with fwhm 1.327, 1.345, and 1.401° for the films reduced at 50, 100, and 150 °C, respectively. This peak was slightly shifted toward higher angles with the reduction temperature, which may decrease the interlayer

spacing. Interlayer spacing in GO was possibly reduced due to the evaporation of oxygen links between the basal planes.[18] However, it is observed that with the increment of reduction degrees, the peak gets weak and broad, and it indicates a change from a bigger flake structure to a micro-granular carbon
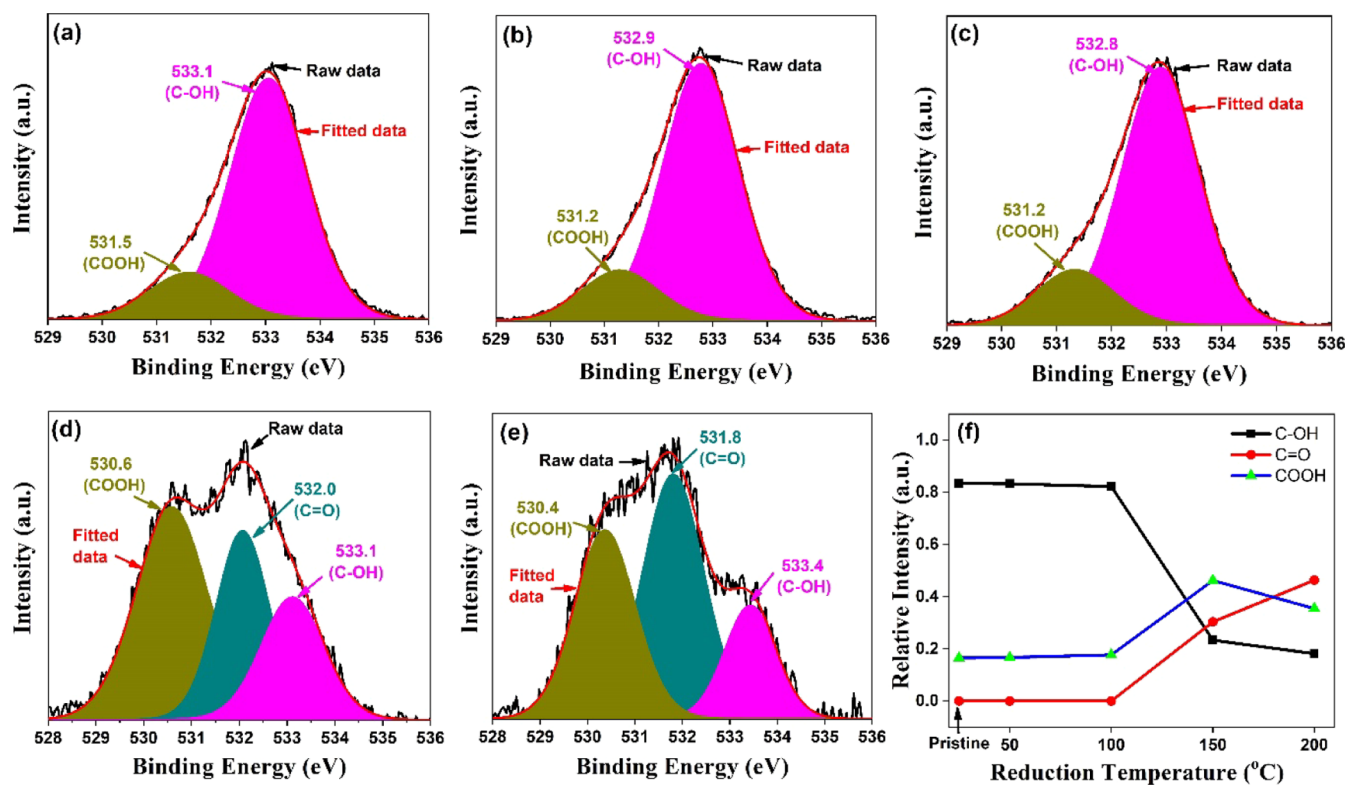
Figure 4. Deconvoluted high-resolution O_{1s} spectra for (a) pristine and the samples reduced at (b) 50, (c) 100 (d) 150, (e) 200 °C; (f) reduction dependence of the relative contribution of O_{1s} peak components.

Table 1. Reduction Dependence of the Relative Percentage Contribution of Different Functional Groups and the Relative Percentage Elemental Composition Estimated by Full Scan Spectra

	group	pristine	50 °C	100 °C	150 °C	200 °C
elemental composition (%)	C	75.43	75.62	76.24	83.86	89.83
	O	24.57	24.38	23.76	16.14	10.17
	C=C/C−C	30.05	36.43	40.72	71.53	83.16
C_{1S} deconvolution	C−OH	27.15	20.14	18.88	14.86	8.20
	>C=O	35.33	32.74	31.65	9.32	5.11
	−COOH	10.05	8.75	8.09	4.29	3.54
O_{1S} deconvolution	−COOH	16.53	16.72	17.72	46.25	35.45
	>C=O				30.38	46.39
	C−OH	83.47	83.28	82.28	23.36	18.16

matrix. However, the film reduced at 200 °C shows a broad peak around 22° (2θ) corresponding to (002) planes of the graphite framework.[18,19] At such a higher degree of reduction, the deterioration of (001) meanwhile arising of the (002) illustrates the domination of graphite structure over graphene oxide (GO).

Figure 2 shows the Raman spectra of deposited GO and rGO thin films. Raman spectroscopy is a powerful tool to extract the identification of the GO samples, including the structural disorder defects, crystallization, and amount of carbon present during oxidation and reduction. The two major peaks at 1314 and 1591 cm^{-1}, corresponding to the D-band and G-band, are observed clearly. Raman spectra of carbon-based materials are due to (i) the D-band being related to the disorder and defects in the hexagonal lattice and (ii) vibration mode for sp^2 carbons atoms (G-band), which occurs owing to C−C stretching.[20] The integrated intensity I_D/I_G ratio (calculated by dividing the area covered by the peaks, obtained from the origin peak fitting) slightly initially decreased from

1.89, calculated for the pristine sample, to 1.81, 1.78, and 1.75, with increase of the reduction temperature as 50, 100, and 150 °C, respectively. It indicates the removal of oxygen functionalities due to vacuum annealing and lesser defects on the surface of rGO.[20] The I_D/I_G ratio significantly increased to 2.22 for the sample reduced at 200 °C. The increase in the I_D/I_G ratio is ascribed to an increase in the number and/or the size of sp^2 clusters,[21] and it may be due to the domination of the graphite matrix. A less-intense band was also observed in the Raman spectra at ∼2700 cm^{-1}. This 2D band is the assertion of graphene structure and may provide information about the number of layers in GO sheets.[21]

The atomic concentration and evolution of surface functionalization were determined by XPS. The full scan XPS survey analysis was carried out for atomic concentration, and high-resolution spectra of C_{1s} and O_{1s} were carried out for quantitative analysis of surface functionalities. The deconvolution of C_{1s} and O_{1s} spectra was performed using Casa XPS software with Shirley background correction. Figure 3 shows
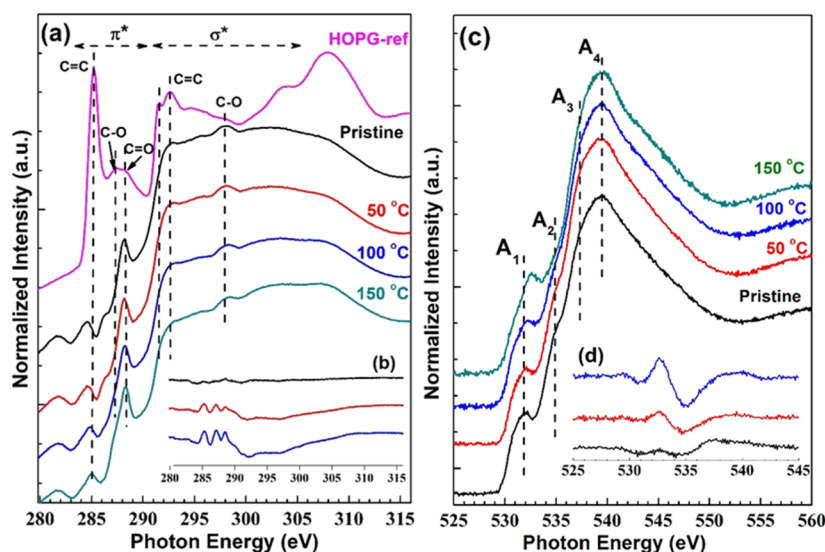
Figure 5. Normalized NEXAFS for GO and rGO films: (a) C K-edge, (b) C K-edge difference spectra, (c) O K-edge, and (d) O K-edge difference spectra.

high-resolution C_{1s} spectra. The deconvoluted peaks of the C_{1s} spectrum of GO consist of four broad components. The component at 284.7 eV is attributed to the sp^2 component (C=C/C−C). The component at 285.4 eV is attributed to hydroxyl configuration (C−OH). The components at 287.3 and 288.6 eV are assigned to carbonyl (>C=O) and carboxyl groups (COOH or OH−C=O). The high-resolution O_{1s} are shown in Figure 4. The deconvoluted peaks of the O_{1s} spectrum with binding energies (BE) 531.5, 532.0, and 533.1 eV represent −COOH (HO−C=O), >C=O, and C−OH, groups, respectively. The relative intensity of peak C−OH exhibits an initial increase at 50 °C (Table 1), which is most possibly due to the internal conversion of OH−C=O to C−OH.[22] The shift of sp^2 peak-maxima back to lower BE with increasing temperature signifies the transformation of electrically insulated GO to the conducting nature of graphite.

The relative intensity of the sp^2 component (C=C/C−C) increases as the reduction temperature increases, and an associated decrease of the oxygen groups (Table 1) confirms the reduction of GO as shown in Figures 3f and 4f, which agrees with the results demonstrated by Gaashani et al. and Bai et al.[22,23]

The NEXAFS spectra in the total electron yield (TEY) mode at the K-edge of principal constituents C and O are shown in Figure 5a,c, respectively. Meanwhile, the difference spectra are shown in the inset of these figures. The spectra were recorded at 90° incidence of the linear polarized X-ray beam. The NEXAFS measurement is an effective method for analyzing the unoccupied electronic structure of carbon-related materials. Furthermore, NEXAFS provides information about hetero generations in local structure, chemical bonding configurations, and nearest/next neighbor environment.

The resonance peaks for $1s−\pi^*$ and $1s−\sigma^*$ are located for the carbon K-edge NEXAFS observed around ∼285 and ∼293 eV, respectively. The spectral features for the carbon K-edge in the TEY mode are displayed in Table 2. The recorded spectra at the carbon K-edge are compared with standard spectra for highly ordered pyrolytic graphite (HOPG). The strong 2D geometry in the ideal structure of the graphite matrix is supposed to have strong directionality of the orbitals: hence, r-orbitals lie within the basal plane, and p-orbitals are directed

Table 2. Spectral Features for the Carbon K-Edge in the TEY Mode

photon energy (eV)	NEXAFS spectral feature
285.2	excitation of carbon in the sp^2 network into the π^* bond
286.5	π^* excitation for carbon that is single bonded to oxygen either in hydroxyl or in epoxy configuration/functional groups
288.7	C=O, a π^* resonance in carboxyl groups
291.6	σ resonance is broader, and absence of core excitation defects, the sp^2 network
292.6	σ^* resonance for un-interrupted sp^2 network
297.5	σ^* resonance attribute to single-bonded oxygen
330	strong functionalization and interference with many states, C=O sigma features from carboxyl expected cannot be resolved (usually not shown in spectra)

perpendicular to the basal plane. For the sp^2 hybridized carbon structure, the sigma bond lies in the plane of the structure, and the pi-bond exists out of the plane (in the perpendicular basal plane), so the E- vector of X-rays must be parallel for perpendicular incidence to the highly ordered graphene structure. As a result, the intensity of the $1s−\pi^*$ transition should be extremely poor compared to $1s−\sigma^*$. However, the observed intensity of π^* in recorded spectra compared to HOPG suggests that the synthesized GO and rGO do not possess a perfectly plane structure. It may be due to the coexistence of different micro-domains and disordered stacking of GO and rGO planes contrasted to HOPG and the disorder induced by the oxidation processes. Moreover, the hydroxyl and epoxy groups dispersed randomly on the top and bottom of the basal plane of each graphene coating would draw the bonded carbon atoms up and down concerning the basal plane. The $1s−\sigma^*$ transition observed with a broad peak compared to HOPG also implies a defective sp^2 geometry.

The transition observed at 288.7 eV related to π^* resonance in the carboxyl group (>C=O, shown by the arrow in Figure 5a), is intensified with reduction temperature; this relative change can be observed from the difference spectra shown in the inset of Figure 5b and result in the gradual reduction of GO. A shoulder peak of ∼292 eV of rGO should be an excitonic state; the presence of this excitonic state implies that

rGO consists of too many sp^2 hybridized carbon atoms, as this peak is commonly observed for pristine graphite.[24]

The XAS spectra for the K edge of O_{1S} are recorded with two clear resonance peaks at ~532 and ~540 eV (Figure 5c). The peak around 532 eV could be assigned to π^* resonances, and the peak around 540 eV is possible from σ^* resonances of the carbonyl group ($-C=O$).[24,25] Spectral features of the O−K edge (A_1, A_2, A_3, and A_4) are shown in Table 3. The

Table 3. Spectral Features for the Oxygen K-Edge in the TEY Mode

peak	photon energy (eV)	NEXAFS spectral feature
A_1	531.88	π^* resonances from oxygen double bonded to carbon ($C=O$)[26,27]
A_2	535.10	σ^* (O−H)[27,28]
A_3	537.43	σ^* related to C−OH and C−O−C[26,27]
A_4	539.34	σ^* related to C=O[27]

intensities of both transitions are notably affected by the reduction temperature, as can be seen clearly from the difference spectra (Figure 5d), and it leads to the tunable

defunctionalization of GO. NEXAFS spectra suggested relatively higher degrees of recoveries of π-conjugation upon reduction.

The angle dependence NEXFAS spectra recorded in the PEF mode are shown in Figure 6. It can be observed from the spectra that synthesized samples are isotropic.

Figure 7a−e shows the Kelvin probe microscope spectra of pristine GO and rGO thin films thermally reduced at 50, 100, 150, and 200 °C, respectively. SKPM is a modified version of atomic force microscopy, which provides non-destructive and non-contact topography of the sample, including the contact potential difference between a sample and the tip. The SKPM is employed to determine the work function of these films. For this purpose, one set of films was deposited on FTO-coated glass substrates and annealed along with other samples. It provides desired measurement results without introducing extra effects due to Schottky barrier formation.[29,30] It is well known that the work function depends on the carrier concentrations. Hence, tuning GO from semiconductor to metallic work function will have an expected response. Scanning probe methods such as SKPM provide spatial resolution and allow the detection of local surface potentials.[30] In general, V_{kelvin} is the voltage needed to compensate for the
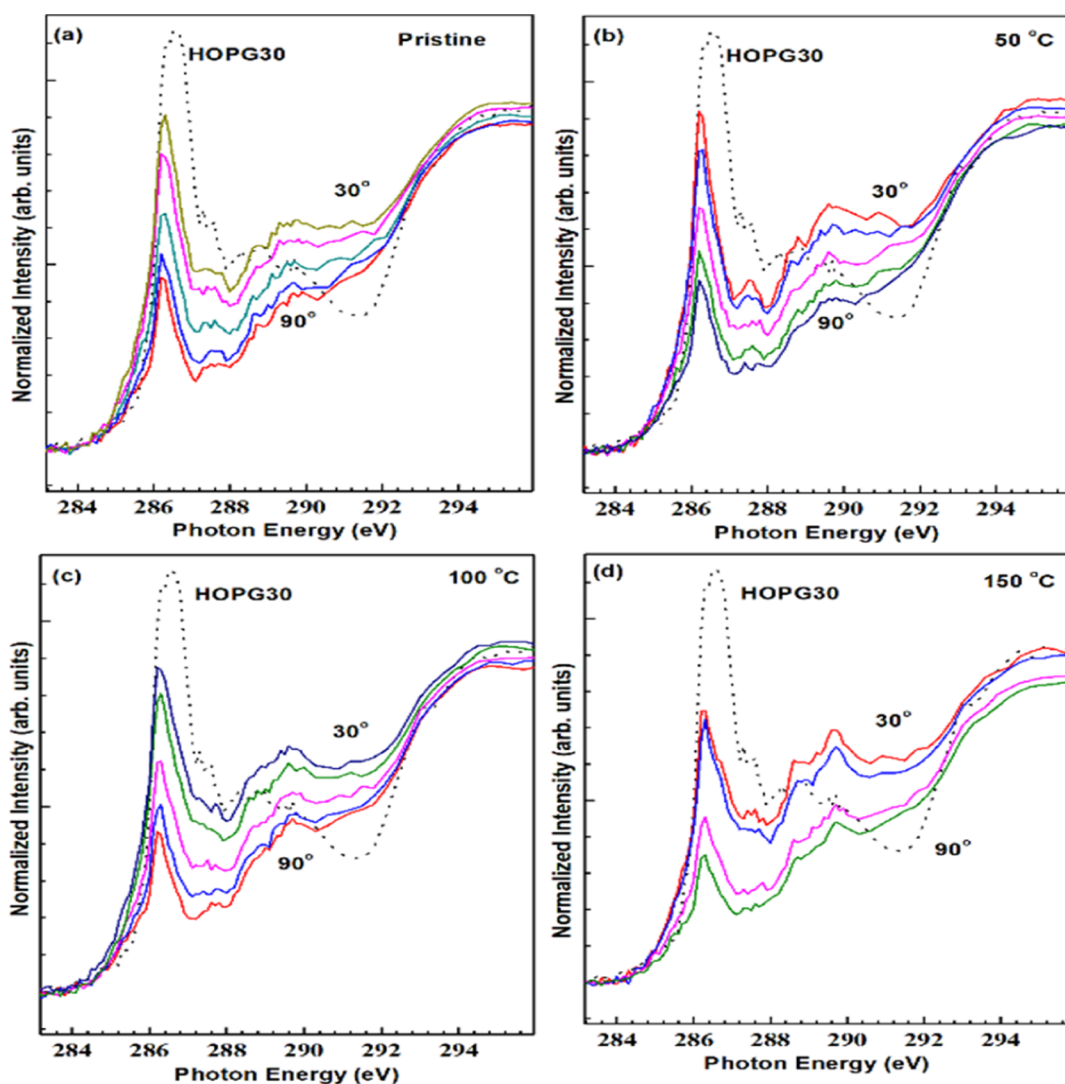

Figure 6. Angle dependence of the GO samples in the PEY mode (a) pristine, and reduced at (b) 50, (c) 100, and (d) 150 °C.
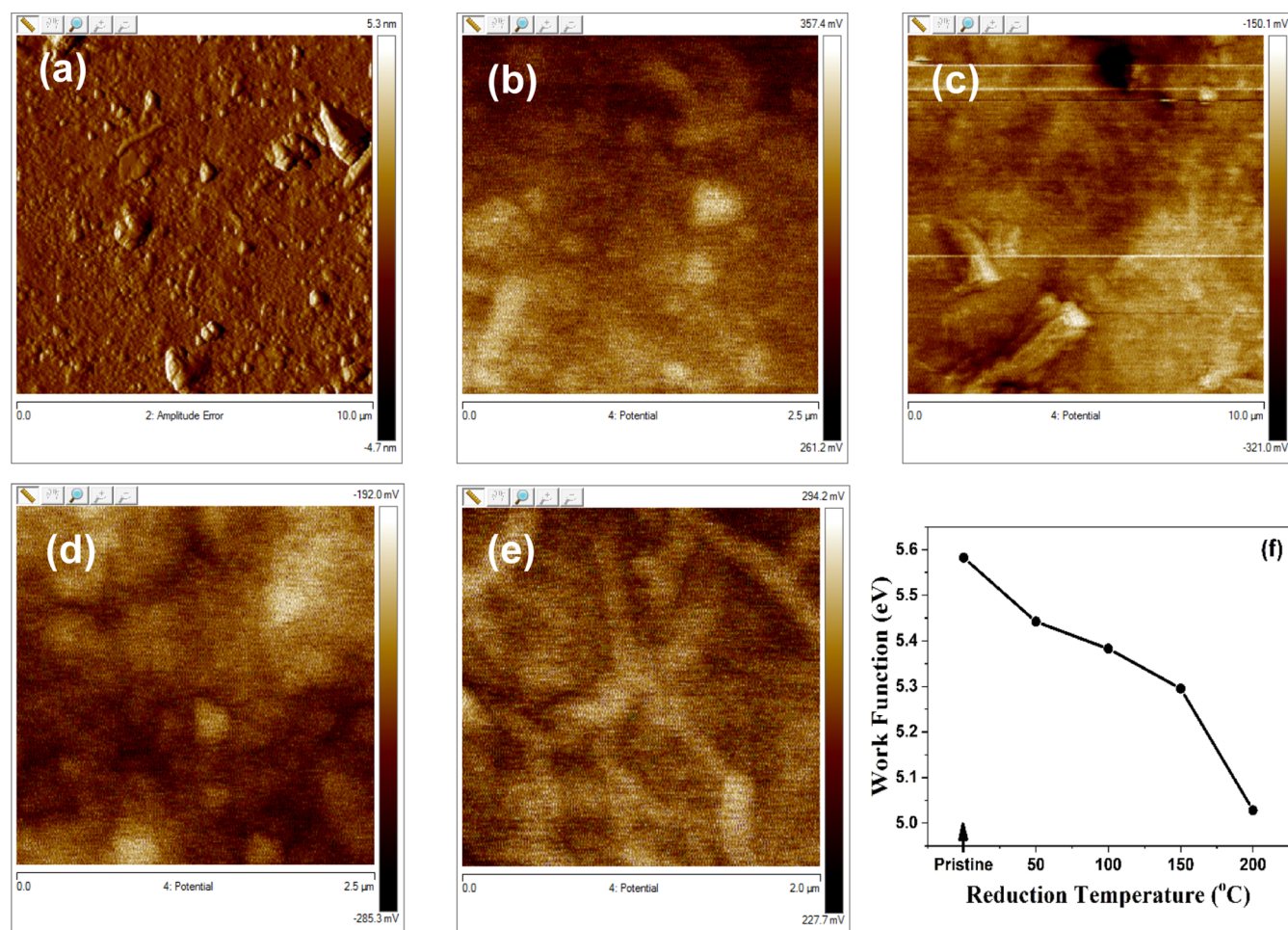
Figure 7. SKPM images of GO and rGO thin films (a) pristine, (b) 50, (c) 100, (d) 150, (e) 200 °C, and (f) work function calculated from Kelvin probe microscope spectra.

non-biased setup ($V_{bias} = 0$), and V_{kelvin} is equal to the contact potential difference between the tip and the sample.[31]

$$V_{CPD} = \frac{1}{e}(\phi_{tip} - \phi_{sample})$$

where Φ_{tip} and Φ_{sample} are the work functions of the tip and sample, respectively, and e is the elementary charge. This method is implied to investigate the surface potential of GO thin films on FTO-coated glass substrates.

During the measurements of surface potential scans, Gaussian distribution is considered due to typical disorder in a polycrystalline carbonaceous semiconductor thin film.[32] The work function is measured at around 5.58 eV for the pristine GO; meanwhile, it is decreased with a reduction grade of GO (shown in Figure 7f), with the values 5.44, 5.38, 5.29, and 5.03 eV for the samples reduced at 50, 100, 150, and 200 °C, respectively. The reduction in the work function may be a possible reason to enhance the charge transport property of GO.

The UV−vis absorption spectrum of aqueous GO dispersion is shown in Figure S2 (Supporting Information). The pristine GO shows two kinds of characteristic features: a major peak is observed at ~235 nm due to $\pi−\pi^*$ transitions of aromatic ring electrons related to C═C and C−C bonds. Another characteristic shoulder peak at ~307 nm corresponds to the n−π^* transitions of the carbonyl group (C═O) electrons.[33]

The band gap is evaluated by employing Tauc plots (shown in the inset of Figure S2) for the spectra to fit the data, assuming $\alpha^{1/2} = (h\nu − E_g)$ relationship corresponding to the indirect transitions, where "α" is the absorption coefficient and "$h\nu$" is photon energy.[34] The sharp adsorption edges were not observed in the Tauc plots due to the domination of the less-arranged carbon matrix and non-uniform oxidation levels in GO itself. The band gap is measured at around 2.76 eV for the pristine one, which is inconsistent with the reported indirect band gap for GO.[34,35] Meanwhile, the band gap shrinkage is significant with values of 2.35, 2.12, 1.24, and 0.79 eV for the samples reduced at 50, 100, 150, and 200 °C, respectively.

The surface morphology of pristine GO and rGO films (thermally reduced at 50, 100, 150, and 200 °C) analyzed by FESEM is shown in Figure S3a−e (Supporting Information). The reduction process can reduce as well as exfoliate the pristine GO into fluffy and wrinkled rGO, which can be observed. The deformation of rGO observed in FESEM images is mostly due to the elimination of oxygen-containing groups from the carbon planes during the reduction. The wrinkled structure offers a maximum accessible surface area of rGO to occupy the charge carriers from TiO₂. The samples were reduced at 150 °C, and higher temperatures were noticed with tiny-granular morphology instead of flakes as was observed in the pristine one. The granular microstructure enhances the
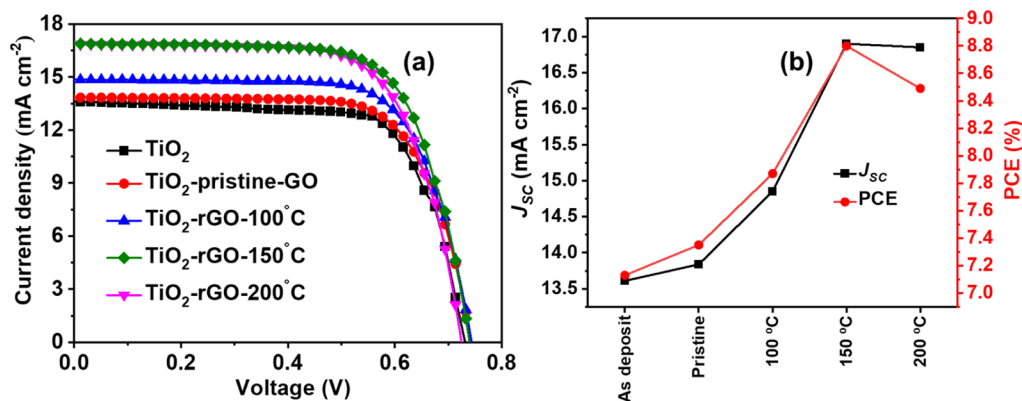
Figure 8. (a) $J-V$ curve of DSSCs using GO/rGO photoanodes and (b) J_{SC} and PCE of DSSC with reduction temperature.

surface-to-volume ratio and further assists in improving the charge transfer. The absence of charging during SEM imaging suggests the relative electrically conductive behavior of rGO, which is related to the electron charge transport property of rGO.[36]

3.2. Photovoltaic Performance. The current density−voltage ($J-V$) curve of DSSCs using GO and rGO are shown in Figure 8a, with Table 4 giving detailed parameters. The J_{SC}

Table 4. Photovoltaic Parameters of DSSCs

DSSC	J_{SC} (mA cm^{-2})	V_{OC} (mV)	FF (%)	PCE (%)
TiO$_2$	13.61	731	71.7	7.13 ± 0.09
TiO$_2$-pristine GO	13.84	743	71.5	7.35 ± 0.10
TiO$_2$-rGO-100 °C	14.85	743	71.4	7.87 ± 0.09
TiO$_2$-rGO-150 °C	16.90	739	70.5	8.80 ± 0.08
TiO$_2$-rGO-200 °C	16.85	725	69.5	8.49 ± 0.10

of DSSCs using TiO$_2$ photoanode is 13.6 mA cm^{-2}, with a PCE of 7.13%. After the addition of pristine GO into the TiO$_2$ photoanode, there is a slight enhancement in J_{SC}, with a PCE of 7.35%. rGO-based TiO$_2$ photoanodes yield further enhancement in J_{SC} and PCE, with the values being dependent on reduction treatment temperature as explained below.

The DSSCs with TiO$_2$-rGO-150 °C exhibited the highest J_{SC} of 16.90 mA cm^{-2} and the highest PCE of 8.80% compared to as-deposited DSSC. The addition of GO/r-GO into the TiO$_2$ photoanode improves the charge transport and acts as a pathway for charge transfer.[21,37] The reduction of GO at the appropriate level as here for 150 °C may be the key reason to adjust the energy level of GO CB energy that implies a higher driven force to push the electron from TiO$_2$ to improve the charge transfer. DSSCs with the composite photoanode (TiO$_2$-rGO-150 °C) also effectively suppress the charge recombination and the back reaction of the photoelectron, which diminishes the diffuse barrier to photoelectron transfer and improves the overall improved performance of the DSSC. The optimum level of oxygen, optical properties, and microstructure seems to occur for improving the performance of DSSCs with rGO-150 °C. The performance of DSSCs with rGO-200 °C decreases due to changes in the phase formation of rGO taking place. There is a slight change in the V_{OC} of rGO-150 °C and rGO-200 °C, and it is due to the change in the work function. Figure 8b shows the change in J_{SC} and PCE with respect to the reduction temperature of GO. J_{SC} of DSSCs increases to 150 °C reduction temperature compared to as-deposited DSSCs. J_{SC} starts decreasing at 200 °C due to

changes in the microstructure and graphite-like phase formation (as discussed in the earlier section).

4. CONCLUSIONS

Modified Hummers method was employed for the synthesis of GO. Thin films coated on corning glass substrates as well as synthesized GO powder were gradually reduced by the vacuum annealing process at four different temperatures (50, 100, 150, and 200 °C). It is observed that the pristine structure turned from a semiconductor to a graphite matrix with the reduction, and it significantly affects the optical, microstructural, and electronic structure and hence the charge transfer properties of GO. It is found that there are anomalous changes in the properties of GO with a reduction of around 150 °C. At lower degrees of reduction (pristine level), the GO layers with a fluffy microstructure and poor charge transfer. On the other hand, at a very high reduction (200 °C), a graphite-like layer is created. With the selection of an appropriate reduction treatment, the maximum advantages can be granted to the GO properties. The DSSCs fabricated with an optimized photoanode having a mesoporous TiO$_2$ mixed with GO nanostructures reduced at 150 °C show the best performance with a J_{SC} of 16.90 mA cm^{-2}, V_{OC} of 739 mV, and FF of 70.5%, with a PCE of 8.80%. Therefore, the incorporation of rGO reduced at the optimum level can play an essential role in improving the DSSC performance.

■ ASSOCIATED CONTENT

⊙ Supporting Information

The Supporting Information is available free of charge at https://pubs.acs.org/doi/10.1021/acsomega.2c05637.

> Various characterization instruments, comparative detail of photovoltaic parameters of DSSCs with GO synthesized using different techniques as reported in the literature, schematic of the charge flow in DSSCs, absorption spectra of aqueous GO dispersion with Tauc plots for the deposited GO and rGO thin films, and FESEM images of GO and rGO films (PDF)

■ AUTHOR INFORMATION

Corresponding Authors

Amanpal Singh − *Department of Physics, University of Rajasthan, Jaipur 302004, India;* ⦿ orcid.org/0000-0001-9106-3565; Email: amanbkn@gmail.com

Sanjay Kumar Swami − *Department of Advanced Components and Materials Engineering, Sunchon National*

University, Suncheon 57922, Republic of Korea;
orcid.org/0000-0002-9156-8317; Email: swami.phy@
gmail.com

Authors

Yogesh Kumar Saini − Department of Physics, University of
Rajasthan, Jaipur 302004, India

Anuj Kumar − Department of Physics, J.C. Bose University of
Science and Technology, YMCA, Faridabad, Haryana
121006, India

Sanjeev Gautam − Advanced Functional Materials
Laboratory, Dr S. S. Bhatnagar University Institute of
Chemical Engineering & Technology, Panjab University,
Chandigarh 160014, India; orcid.org/0000-0003-3123-
9906

Dinesh Kumar − Gurugram University, Gurugram, Haryana
122003, India

Viresh Dutta − Photovoltaic Lab, Department of Energy
Science and Engineering, Indian Institute of Technology Delhi,
New Delhi 110016, India

Han-koo Lee − Pohang Accelerator Laboratory, POSTECH,
Pohang 37673, Republic of Korea

Jongsu Lee − Department of Advanced Components and
Materials Engineering, Sunchon National University,
Suncheon 57922, Republic of Korea

Complete contact information is available at:
https://pubs.acs.org/10.1021/acsomega.2c05637

Notes

The authors declare no competing financial interest.

■ REFERENCES

(1) Wang, J. T. W.; Ball, J. M.; Barea, E. M.; Abate, A.; Alexander-Webber, J. A.; Huang, J.; Saliba, M.; Mora-Sero, I.; Bisquert, J.; Snaith, H. J.; Nicholas, R. J. Low-Temperature Processed Electron Collection Layers of Graphene/TiO$_2$ Nanocomposites in Thin Film Perovskite Solar Cells. Nano Lett. 2014, 14, 724−730.

(2) Kokkonen, M.; Talebi, P.; Zhou, J.; Asgari, S.; Soomro, S. A.; Elsehrawy, F.; Halme, J.; Ahmad, S.; Hagfeldt, A.; Hashmi, S. G. Advanced Research Trends in Dye-Sensitized Solar Cells. J. Mater. Chem. A 2021, 9, 10527−10545.

(3) Dong, P.; Zhu, Y.; Zhang, J.; Peng, C.; Yan, Z.; Li, L.; Peng, Z.; Ruan, G.; Xiao, W.; Lin, H.; Tour, J. M.; Lou, J. Graphene on Metal Grids as the Transparent Conductive Material for Dye Sensitized Solar Cell. J. Phys. Chem. C 2014, 118, 25863−25868.

(4) Ziaeifar, F.; Alizadeh, A.; Shariatinia, Z. Dye Sensitized Solar Cells Fabricated Based on Nanocomposite Photoanodes of TiO$_2$ and AlMo$_{0.5}$O$_3$ Perovskite Nanoparticles. Sol. Energy 2021, 218, 435−444.

(5) Wei, L.; Chen, S.; Yang, Y.; Dong, Y.; Song, W.; Fan, R. Reduced Graphene Oxide Modified TiO$_2$ Semiconductor Materials for Dye-Sensitized Solar Cells. RSC Adv. 2016, 6, 100866−100875.

(6) Bell, N. J.; Du, A.; Ng, Y. H.; Coster, H.; Smith, S. C.; Amal, R. Understanding the Enhancement in Photoelectrochemical Properties of Photocatalytically Prepared TiO$_2$-Reduced Graphene Oxide Composite. J. Phys. Chem. C 2011, 115, 6004−6009.

(7) Muchuweni, E.; Martincigh, B. S.; Nyamori, V. O. Recent Advances in Graphene-Based Materials for Dye-Sensitized Solar Cell Fabrication. RSC Adv. 2020, 10, 44453−44469.

(8) Roy-Mayhew, J. D.; Aksay, I. A. Graphene Materials and Their Use in Dye-Sensitized Solar Cells. Chem. Rev. 2014, 114, 6323−6348.

(9) Yang, N.; Zhai, J.; Wang, D.; Chen, Y.; Jiang, L. Two-Dimensional Graphene Bridges Enhanced Photoinduced Charge Transport in Dye-Sensitized Solar Cells. ACS Nano 2010, 4, 887−894.

(10) Min, S.; Lu, G. Dye-Sensitized Reduced Graphene Oxide Photocatalysts for Highly Efficient Visible-Light-Driven Water Reduction. J. Phys. Chem. C 2011, 115, 13938−13945.

(11) Jo, J.; Lee, S.; Gim, J.; Song, J.; Kim, S.; Mathew, V.; Alfaruqi, M. H.; Kim, S.; Lim, J.; Kim, J. Facile Synthesis of Reduced Graphene Oxide by Modified Hummer's Method as Anode Material for Li-, Na- and K-Ion Secondary Batteries. R. Soc. Open Sci. 2019, 6, 181978.

(12) Toe, M. Z.; Pung, S. Y.; Yaacob, K. A.; Matsuda, A.; Tan, W. K.; Han, S. S. Effect of TiO$_2$ Sol on the Conversion Efficiency of TiO$_2$ Based Dye-Sensitized Solar Cell. J. Sol. Gel Sci. Technol. 2020, 95, 439−446.

(13) Sengupta, I.; Chakraborty, S.; Talukdar, M.; Pal, S. K.; Chakraborty, S. Thermal Reduction of Graphene Oxide: How Temperature Influences Purity. J. Mater. Res. 2018, 33, 4113−4122.

(14) Emiru, T. F.; Ayele, D. W. Controlled Synthesis, Character-ization and Reduction of Graphene Oxide: A Convenient Method for Large Scale Production. Egypt. J. Basic Appl. Sci. 2017, 4, 74−79.

(15) Nathabumroong, S.; Poochai, C.; Chanlek, N.; Eknapakul, T.; Sonsupap, S.; Tuichai, W.; Sriprachuabwong, C.; Rujirawat, S.; Songsiriritthigul, P.; Tuantranont, A.; Yimnirun, R. Enhanced Surface and Electrochemical Properties of Nitrogen-Doped Reduced Graphene Oxide by Violet Laser Treatment for High Charge Storage and Lower Self-Discharge Supercapacitors. J. Power Sources 2021, 513, 230517.

(16) Swami, S. K.; Chaturvedi, N.; Kumar, A.; Dutta, V. Dye Sensitized Solar Cells Using the Electric Field Assisted Spray Deposited Kesterite (Cu$_2$ZnSnS$_4$) Films as the Counter Electrodes for Improved Performance. Electrochim. Acta 2018, 263, 26−33.

(17) Swami, S. K.; Chaturvedi, N.; Kumar, A.; Dutta, V. Effect of Zinc Precursor on Cu$_2$ZnSnS$_4$ Nanoparticles Synthesized by the Solvothermal Method and Its Application in Dye-Sensitized Solar Cells as the Counter Electrode. Mater. Today Energy 2018, 9, 377−382.

(18) Jeong, H.-K.; Lee, Y. P.; Lahaye, R. J. W. E.; An, K.-H.; Kim, I. J.; Yang, C. W.; Park, C.-Y.; Park, M.-H.; Ruoff, R. S.; Lee, Y. H. Evidence of Graphitic AB Stacking Order of Graphite Oxides. J. Am. Chem. Soc. 2008, 130, 1362−1366.

(19) Li, Z. Q.; Lu, C. J.; Xia, Z. P.; Zhou, Y.; Luo, Z. X-Ray Diffraction Patterns of Graphite and Turbostratic Carbon. Carbon 2007, 45, 1686−1695.

(20) Mondal, J.; Srivastava, S. δ-MnO$_2$ Nanoflowers and Their Reduced Graphene Oxide Nanocomposites for Electromagnetic Interference Shielding. ACS Appl. Nano Mater. 2020, 3, 11048−11059.

(21) Cheng, G.; Akhtar, M. S.; Yang, O.-B.; Stadler, F. J. Novel Preparation of Anatase TiO$_2$@Reduced Graphene Oxide Hybrids for High-Performance Dye-Sensitized Solar Cells. ACS Appl. Mater. Interfaces 2013, 5, 6635−6642.

(22) Al-Gaashani, R.; Najjar, A.; Zakaria, Y.; Mansour, S.; Atieh, M. A. XPS and Structural Studies of High Quality Graphene Oxide and Reduced Graphene Oxide Prepared by Different Chemical Oxidation Methods. Ceram. Int. 2019, 45, 14439−14448.

(23) Bai, L.; Xu, Y.; Liu, A.; Dong, L.; Zhang, K.; Li, W. S.; Zhao, F. G. Unusual Graphite Fluoride Hydrolysis toward Unconventional Graphene Oxide for High-Performance Supercapacitors and Li-Ion Batteries. Chem. Eng. J. 2022, 434, 134639.

(24) Yadav, A. K.; Padma, N.; Ghorai, G.; Sahoo, P. K.; Rao, R.; Banerjee, S.; Rajarajan, A. K.; Kumar, P.; Jha, S. N.; Bhattacharyya, D. Local Structural Investigations of Graphitic ZnO and Reduced Graphene Oxide Composite. Appl. Surf. Sci. 2021, 565, 150548.

(25) Lee, V.; Dennis, R. v.; Jaye, C.; Wang, X.; Fischer, D. A.; Cartwright, A. N.; Banerjee, S. In Situ Near-Edge x-Ray Absorption Fine Structure Spectroscopy Investigation of the Thermal Defunctionalization of Graphene Oxide. *J. Vac. Sci. Technol., B* **2012**, *30*, 061206.

(26) Outka, D. A.; Stöhr, J.; Madix, R. J.; Rotermund, H. H.; Hermsmeier, B.; Solomon, J. NEXAFS Studies of Complex Alcohols and Carboxylic Acids on the Si(111)(7×7) Surface. *Surf. Sci.* **1987**, *185*, 53−74.

(27) Gandhiraman, R. P.; Javier, C.; Koehne, J. E.; Chen, B.; Nordlund, D.; Meyyappan, M. X-ray Absorption Study of Graphene Oxide and Transition Metal Oxide Nanocomposites. *J. Phys. Chem. C* **2014**, *118*, 18706−18712.

(28) Pacilé, D.; Meyer, J. C.; Fraile Rodríguez, A.; Papagno, M.; Gómez-Navarro, C.; Sundaram, R. S.; Burghard, M.; Kern, K.; Carbone, C.; Kaiser, U. Electronic Properties and Atomic Structure of Graphene Oxide Membranes. *Carbon* **2011**, *49*, 966−972.

(29) Ramamoorthy, H.; Buapan, K.; Chiawchan, T.; Thamkrongart, K.; Somphonsane, R. Exploration of the Temperature-Dependent Correlations Present in the Structural, Morphological and Electrical Properties of Thermally Reduced Free-Standing Graphene Oxide Papers. *J. Mater. Sci.* **2021**, *56*, 15134−15150.

(30) Maragliano, C.; Lilliu, S.; Dahlem, M. S.; Chiesa, M.; Souier, T.; Stefancich, M. Quantifying Charge Carrier Concentration in ZnO Thin Films by Scanning Kelvin Probe Microscopy. *Sci. Rep.* **2014**, *4*, 1−7.

(31) Druga, T.; Wenderoth, M.; Lüpke, F.; Ulbrich, R. G. Graphene-Metal Contact Resistivity on Semi-Insulating 6H-SiC(0001) Measured with Kelvin Probe Force Microscopy. *Appl. Phys. Lett.* **2013**, *103*, 051601.

(32) Bässler, H. Charge Transport in Disordered Organic Photoconductors a Monte Carlo Simulation Study. *Phys. Status Solidi B* **1993**, *175*, 15−56.

(33) Liu, W.; Speranza, G. Tuning the Oxygen Content of Reduced Graphene Oxide and Effects on Its Properties. *ACS Omega* **2021**, *6*, 6195−6205.

(34) Méndez-Romero, U. A.; Pérez-García, S. A.; Xu, X.; Wang, E.; Licea-Jiménez, L. Functionalized Reduced Graphene Oxide with Tunable Band Gap and Good Solubility in Organic Solvents. *Carbon* **2019**, *146*, 491−502.

(35) Hunt, A.; Kurmaev, E. Z.; Moewes, A. Band Gap Engineering of Graphene Oxide by Chemical Modification. *Carbon* **2014**, *75*, 366−371.

(36) Strankowski, M.; Piszczyk, Ł.; Kosmela, P.; Korzeniewski, P. Morphology and the Physical and Thermal Properties of Thermoplastic Polyurethane Reinforced with Thermally Reduced Graphene Oxide. *Pol. J. Chem. Technol.* **2015**, *17*, 88−94.

(37) Peiris, D. S. U.; Ekanayake, P.; Karunaratne, B. A.; Petra, M. I. Improved Performance of DSSC Photoanodes After the Modification of TiO_2 with Reduced Graphene Oxide. *J. Electron. Mater.* **2021**, *50*, 1044−1053.